Resolution and Efficiency of Large Area Picosecond Photo-Detectors

M. Hutchinson
Department of Physics
University of Chicago
Chicago, IL 60637
(Dated: May 31, 2012)

This paper presents large area picosecond photo-detectors (LAPPD) as compelling detectors for neutrino, collider, and medical imaging experiments. The design and functionality of these detectors is described with emphasis on the process of computing the horizontal position of an event, known as second localization. An experimental study of this process in a prototype detector is presented. Ultimately, the prototype is shown to be error prone. An analysis of design space shows begins to characterize future detectors.

Keywords: photo-detector, multi-channel plate, positron-emission tomography

I. INTRODUCTION

A. Motivation

High resolution, high speed photo-detection is essential for modern neutrino experiments, collider experiments, and medical imaging. In neutrino experiments, high speed measurements allow for detection in noisy environments, even above ground. In collider experiments, the temporal resolution needed to measure time-of-flight would enable accurate measurement of particle mass [1]. In medical imaging, high spatial resolution is needed to resolve biological structures, and high speeds to handle high particle flux rates. Positron-Emission Tomography (PET) is a regime of medical imaging that is especially sensitive to high efficiency photo-detection.

PET functions by introducing compounds which have been tagged with positron emitters to the human body. In vivo, the emitted positrons annihilate with electrons in tissue, mostly water, and emit a pair of gammas. Due to conservation of momentum, these gammas exit the body nearly anti-parallel, and can be detected by a number of means.

The efficacy of the PET scheme can be measured in a few ways. First, the size of the dose experienced by the patient is governed by the faction of emitted gammas that are detected and the amount of information gleaned by each detection. Second, the length of the procedure, which affects motion-related blurring of the image and the overall throughput of the facility, is governed by the flux of events the detector can handle. Finally, the turn around time of data is governed by the speed of the data analysis methods. In this regard, there is qualitative difference between pseudo-realtime systems, which allow for on-the-fly adjustments and other doctor-patient interactions, and batch systems, where data processing time inhibits such interactions.

Large area picosecond photo-detectors (LAPPD) could provide the needed resolution and efficiency for PET systems [2][3][4][5]. LAPPD systems have high spatial and temporal resolution, owing to their small feature size and advanced electronics. LAPPD systems are also capable of handing high flux rates as they digitize signals in small batches and are coupled with hardware-based analysis.

At this point in development, experiments are being devised to verify low-level functionality of LAPPD detectors. These experiments are application general thus far, and examine traits like single-event resolution.

B. Outline

In Section 2, a description of the LAPPD apparatus and prototype facility is given. In Section 3, a verification experiment, the measurement of signal propagation speed in the anode, is described and data presented. In Section 4, the data processing procedure is given and and demonstrated on the experimental data. In Section 5, further aspects of the apparatus are discussed and in Section 6, conclusions are drawn.

II. APPARATUS

A large area picosecond photo-detector system has three layers: a physical layer akin to a photomultiplier tube (PMT), an electronics layer akin to a time-to-digital converter (TDC), and a software layer for processing and visualization.

The physical layer consists of a photocathode, microchannel plate (MCP), anode strip-line, and sealed enclosure. The photocathode converts incident photons to electrons. A voltage is applied across the MCP, causing photo-electrons to cascade along the channel walls, amplifying the signal with a gain $G \approx 10^6$. The resulting shower strikes the anode strip-line, sending an electrical pulse down the anode to opposite ends of the enclosure where they are read by the electronics. This process is shown in Figure 3. Multiple enclosures, or tiles, can be arranged in the plane to create a detector panel, or supermodule. The front of one such supermodule can be seen in Figure 2. Events leave the physical layer as two analog electrical pulses at opposite ends of the panel.

The electronics layer consists of an analog card (AC), a digital card (DC), and a central card (CC) [6]. The ana-

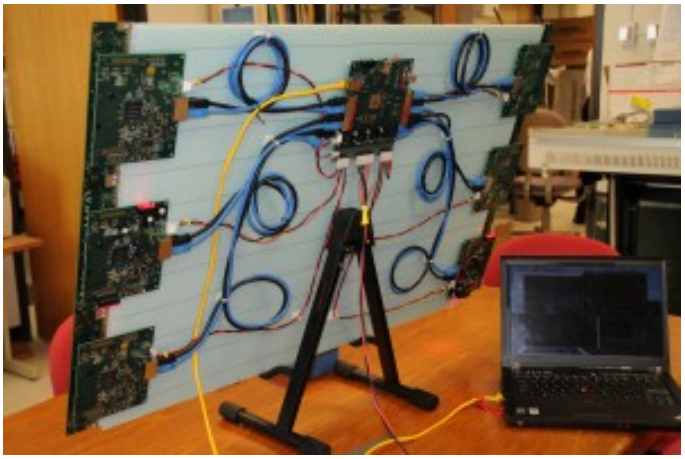

FIG. 1: The back side of the Supermodule, showing the Digital Cards connected to the Analog Cards and to the Central Card (CC). The CC transmits the time, location, and integrated charge of hits to a PCI-E computer containing a teraflop GPU for real-time reconstruction and display. (Photo-credit Rich Northrop)

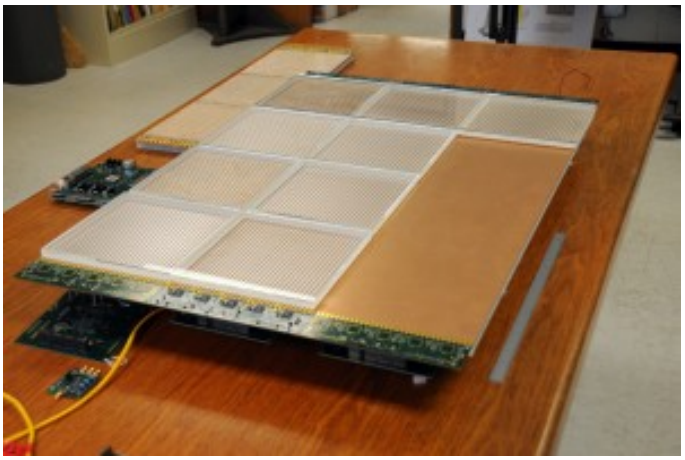

FIG. 2: The front side of the Supermodule, which holds twelve tiles in three rows of four tiles each, sitting on the Tray. Three tiles have been left off so that the strip-line copper ground plane is visible. The Analog Cards are visible on the ends of the tile rows. (Photo credit: Rich Northrop)

log card uses PSEC4 digital oscilloscopes to digitize the incoming pulses at up to 15 Giga-samples/s. The digital card computes the pulse's incident time and center strip-line. This process will be referred to as first localization and the central strip-line of the pulse as it's y or vertical position. The central card pairs pulses from opposite ends of the enclosure and computes the position along the strip line that the electron shower occurred. This process will be referred to as second localization and the position along the strip line as it's x or horizontal position. Events leave the electronics layer as three-vectors: the time and position in the plane of the detector. The electronics can be seen mounted to the back of the supermodule in Figure 1.

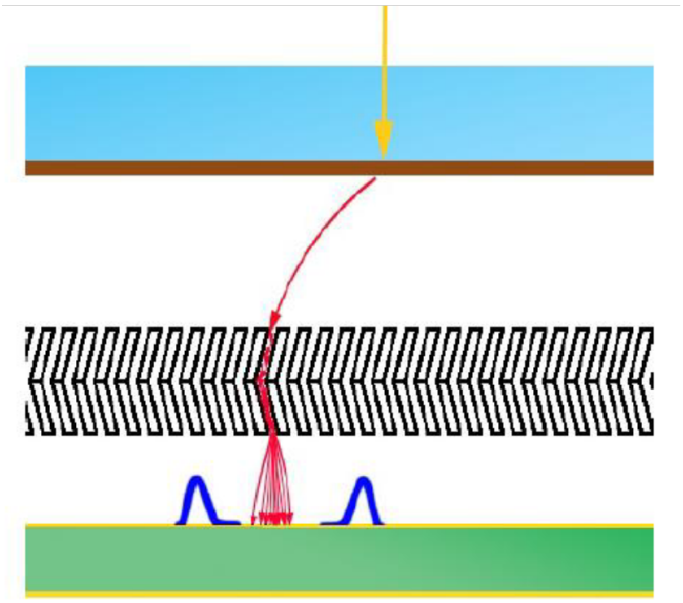

FIG. 3: Sketch of physical layer of the LAPPD system. Incoming photons are shown in yellow, electrons in red, and an electrical signal in blue. The brown layer is the photocathode, the black layer is the double-layer MCP, and the green layer is the anode.

The software layer consists of interface, control, and processing modules. The interface module manages connections to detector enclosures. The control module allows the user to pass commands, e.g. triggers, to the electronics. The processing module performs additional processing based on the target application and visualization.

In this paper, we will discuss two LAPPD setups. The first is a early prototype system at Argonne National Laboratory (ANL), referred to as the evaluation system. In consists of a single 8" physical tile triggered by a foo second UV laser. A single anode strip is read out at both ends by an evaluation board: a PSEC4 chip mounted on a simplified analog card. The raw digital readout is stored for software post-processing, as opposed to hardware post-processing in the full LAPPD setup. Software implementations of the algorithms used in hardware provide rapid verification of the physical layer and a testbed for electronics layer.

The second is a model setup, akin to a detector that would be installed at a neutrino, collider, or medical facility. It consists of 8" tiles arranged three high and four across, for a total of 24" by 32." Each tile has 30 anode lines, for a total of 90 top to bottom, or a density of nearly one line per 2/3 cm. The anodes are read by the PSEC4 chips, 6 channels each, mounted in groups of 5 on the analog card. Each analog card is mounted directly to a digital card for rapid communication. The digital card communicates directly with a central card via serial

Event	t_l (ns)	t_r (ns)	X (mm)
24	12.2 ± 0.3	17.61 ± 0.03	-370 ± 20
84	0.60 ± 0.02	6.0 ± 0.1	-372 ± 7
1035	2.96 ± 0.06	8.41 ± 0.03	-376 ± 4
1080	1.41 ± 0.05	6.80 ± 0.10	-372 ± 8

TABLE I: Example timing data from first localization. This data was collected from the evaluation setup with the laser in the 0 mm position.

Position (mm)	Δt (ns)	Δt, shifted (ns)
-9 mm	-5.338 ± 0.003	$-0.082 \pm .004$
-6 mm	-5.373 ± 0.004	$-0.047 \pm .005$
-3 mm	-5.419 ± 0.006	$-0.001 \pm .007$
0 mm	-5.420 ± 0.003	0
3 mm	-5.550 ± 0.009	$0.130 \pm .009$
6 mm	-5.559 ± 0.009	$0.139 \pm .009$
9 mm	-5.76 ± 0.04	$0.34 \pm .04$

TABLE II: Aggregate data for laser displacement experiment using the evaluation procedure. Uncertainty on the position is $\pm 1 \mu m$.

low-voltage differential signaling at 800 MBit/s. Each central card is connected to 3 pairs of digital cards. The central card communicates with the computer via gigabit ethernet.

III. DATA ACQUISITION

Here, we present early results from a prototype system at the Argonne National Laboratory. The goal of this example experiment is to quantify the accuracy of the first and second localization schemes. The evaluation system is triggered by the UV laser and the resulting pulses recorded. The laser is then translated along the strip-line in 3 mm increments, ranging from -9 to 9 mm in either direction. Although the absolute position of the laser is unknown, comparing to the initial reference measurement allows for quantification of the relative translation. Knowing the propagation speed in the anode, the second localization should detect this translation. Alternatively, one could consider this experiment a measurement of that propagation speed. The data presented here was acquired by Eric Oberla and Andrey Elagin [8].

An example of the evaluation data readout is seen in Figure 4. Each pulse is individually localized: the rising edge is fit yielding a time for the pulse and uncertainty in that time. For a detailed description of the first localization procedure, see [7]. Because the evaluation setup reads out a single anode, the vertical position is neglected. In the evaluation procedure, Aaron Meyer performs the first localization as he sees fit and provides me with a list of times and uncertainties. An example of such values can be seen in Table I.

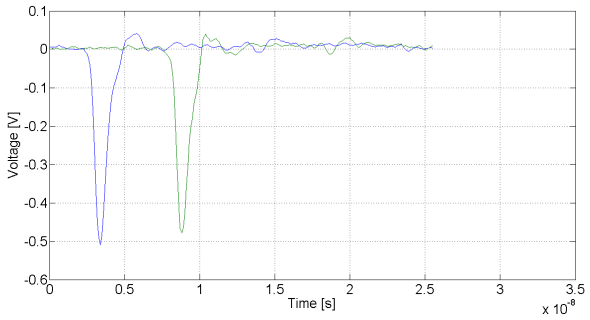

FIG. 4: Pair of signals from a single event as seen by opposite ends of the anode strip-lines [7]

.

Left		Actual		Right
(0,0)	$\longrightarrow$	(0,2,0)	$\longleftarrow$	(0,0)
(1,0)	$\longrightarrow$	(2,0,0)	$\swarrow$	(2,1)
(4,1)	$\longrightarrow$	(3,4,1)	$\nwarrow$	(3,0)
(5,0)	$\longrightarrow$	(5,2,1)	$\longleftarrow$	(5,0)

TABLE III: Event lists demonstrating mismatched events. The Left and Right columns are (t, y) single-ended events and the Actual column is the (t', x', y') three-vector. For simplicity t' is the average of the left and right and x' is the difference plus 2.

IV. DATA ANALYSIS

The digital card passes single-ended events, $(t, y, \sigma_t, \sigma_y)$, to the central card to be paired and localized in the x-axis.

The pairing algorithm takes two lists of single-ended events, one from each side of the detector, and outputs a list of pairs of events. If the incident rate is high enough, the time difference between the right and left of the detector can cause the events to be detected out-of-order. An simple example of this is found in Table III. Additionally, some single-ended events may lose their partner if they are mistakenly discriminated or if the opposite side of the detector is dead during the incidence of the pulse. The role of the pairing algorithm is to search for pairs of single-ended events that are likely to have come from the same physical event and to discard information about unpaired events.

The pairing algorithm employed relies on a fitness function and sliding window. The fitness function takes a left and right single-ended event as input and outputs a real number corresponding to the fitness of the pair, akin to the likelihood they correspond to a physical event. The simplest non-trivial fitness function is $f(y_1, y_2) = \delta_{y_l, y_r}$, which ensures that the single-ended events share a vertical position. A more robust alternative is:

$$f(t_1, y_1, \sigma_{t1}, \sigma_{y1}, t_2, y_2, \sigma_{t2}, \sigma_{y2}) = \frac{1}{1 + |y_1 - y_2|} \quad (1)$$

A copy of the N most recent left and right single sided events, called the buffer, is kept. The events are added in

chronological order based on their single-ended time. If the left or right side of the buffer is full, then the fitness function is applied to each pair of left and right events in the buffer. The pair that results in the highest fitness value is called the candidate. If the candidate's fitness is above a threshold, then the pair is valid, removed from the buffer, and passed to the second localization stage. If no pair has a fitness above the threshold, then the oldest event in the full buffer is removed.

The second localization procedure calculates the actual T, X, Y coordinates of the physical event by looking at the time average and time difference of the ends of the detector. The simplest algorithm is:

$$T = \frac{1}{2}\left[(t_l + t_r) - \frac{W}{c}\right] \tag{2}$$

$$X = \frac{1}{2}\left[c\,(t_l - t_r) + W\right] \tag{3}$$

$$Y = \frac{1}{2}\left[y_l + y_r\right] \tag{4}$$

Adding in error propagation:

$$T = \frac{1}{2}\left[(t_l + t_r) - \frac{W}{c}\right] \tag{5}$$

$$X = \frac{1}{2}\left[c\,(t_l - t_r) + W\right] \tag{6}$$

$$Y = \sigma_Y^2\left[\frac{y_l}{\sigma_{yl}^2} + \frac{y_r}{\sigma_{yr}^2}\right] \tag{7}$$

$$\sigma_T^2 = \frac{1}{2}\left[\sigma_{tl}^2 + \sigma_{tr}^2\right] = \sigma_X^2 \tag{8}$$

$$\sigma_X^2 = \frac{1}{2}\left[\sigma_{tl}^2 + \sigma_{tr}^2\right] = \sigma_T^2 \tag{9}$$

$$\sigma_Y^2 = \left(\sigma_{yl}^{-2} + \sigma_{yr}^{-2}\right)^{-1} \tag{10}$$

The propagation speed in the anode is governed by the anode's glass substrate, which is B33 glass. Our anodes have a dielectric constant around 4.6, corresponding to a propagation speed of $0.46c$.

This procedure is applied to data from the experiment described in Section IV. The aggregate results are found in Table II. Note that in the evaluation setup, this procedure was implemented in software. In future LAPPD systems, it will be implemented in the hardware.

The slope of the linear relationship between the time differences and the displacements is related to the propagation speed. A least-squares fit can be found in Figure 5. The slope of $.021 ns/mm$ corresponds to a speed of $95.2 mm/ns$ or $.318c$.

V. DISCUSSION

The measured and expected values of the propagation speed do not agree well. There are a couple sources of unaccounted for errors. The first is human. The translation table used to create the displacements is digital with

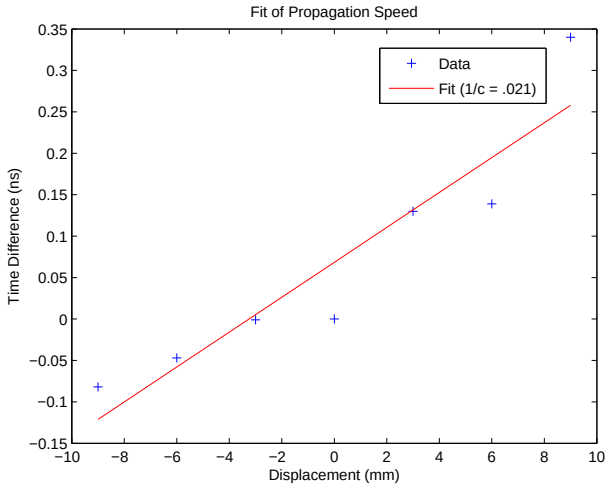

FIG. 5: Least squares fit of the data in Table II.

a very small uncertainty of $1\mu m$, but errors could have been made in inputting the desired translation or labeling the outputs appropriately. The 0 mm displacement stands out as being potentially affected in this way, as it is an outlier that agrees with the -3 mm result. Another source of error is in poor statistics for the 9mm sample. The other samples had order 100 samples each, while it had only 6. Other errors could have been added in the first localization procedure described in [7].

For considering detector design space, it is useful to introduce two concepts: the resolution function and the efficiency function. The resolution function is a map from the configuration space of the LAPPD system to vertical, horizontal, and temporal resolutions. The efficiency function is a map from the configuration space of the LAPPD system to the ratio of the number of events detected to the number of events incident. These two functions characterize the performance of the detector.

The resolution function depends on the intrinsic resolution of the detector and the strength of the two localization steps. The intrinsic resolution is not well understood, noise being the dominating unknown. The first localization is not fully developed. Both are discussed at greater length in [7] and not the topic of this paper.

The second localization procedure serves to propagate the resolutions, or errors, from the first localization step. This propagation was presented in Equations 8, 9, and 10. Assuming uniformity of the left and right side of the detector, the resolutions in X and T are the same as the first localization resolution in t. The Y resolution decreases by a factor of $\sqrt{2}$.

$$\sigma_T = \sigma_X = \sigma_t \qquad \sigma_Y = \frac{\sigma_y}{\sqrt{2}} \tag{11}$$

The efficiency function depends on the dead time and size of the detector, the efficiency of the photo-cathode, and the pairing algorithm. The efficiency can be quan-

tified by considering circumstances in which information is lost.

The first means of loss is when the photo-cathode either fails to produce a photo-electron or produces too few to cascade into a detectable signal. Let the probability that the photo-cathode fails in either mode be P_c.

The second means of loss is when the electronics are unable to record the signal due to 'dead-time', a period after recording data during which the electronics are unable to record more data. Let this time be τ_d. If the areal flux is Φ_A, the supermodule area is A and the number of strip-lines is N, then the probability of an event occurring during dead-time is approximately:

$$P_d \approx \frac{\Phi_A A}{N}\tau_d \tag{12}$$

where the approximation only holds for small P_d, as it only considers two-event dead-times.

The third means of loss is when two events are indistinguishable to the pairing algorithm. Using the pairing algorithm described in Equation 1 and discrete vertical positions, this occurs when two events hit the same strip-line in the same ADC sample. If the length of each sample is τ_s, then the probability of this type of failure is approximately:

$$P_p \approx \frac{\Phi_A A}{N}\tau_s \tag{13}$$

where the approximation only holds for small P_p, as it only considers two-event coincidence. Improvements to the pairing algorithm, including consideration of continuous vertical coordinates, a comparison of pulse shapes or integrated charges, or known incidence patterns, could improve this factor.

Putting these three failure modes together, we can write the efficiency as:

$$f = 1 - P_c - (1 - P_c)\frac{\Phi_A A}{N}(\tau_d + \tau_s) \tag{14}$$

The present prototype is not well suited for testing the pairing procedure. There is only a single source, and a single position and time, triggered such that each sample has a single pulse.

In the future, it would be interesting to add a second laser and translation table to the setup. This would allow for quantification of the minimum separation in position and time of two pulses for them to be decoupled in the electronics. There would almost certainly be an angular dependence which could be complicated. This experiment would better characterize the performance of the detector in high flux situations such as PET.

VI. CONCLUSIONS

The experimental data and processing techniques described here and in [7] were unable to accurately reconstruct the propagation time of signals in the anode. However, they did demonstrate the qualitative behavior of the detector and serve as a proof of concept. Improvements must be made to the prototype to better control avoidable errors such as noise and human error. This would allow more rigorous characterization of the prototype detector in the future.

The second localization procedure propagates uncertainties, and thus resolutions, as described in Equation 11. The temporal and horizontal resolutions are the same as the digital card's temporal resolution, and the vertical resolution decreases by a factor of $\sqrt{2}$ compared to the single-ended value.

The efficiency of the LAPPD system is controlled by the photo-cathode efficiency, the event flux, the size of the detector, the number of strip-lines, the dead-time, and the sample time. Long dead times can be compensated for by thin strip-lines. Low-flux experiments shift focus away from the electronics and to the photo-cathode efficiency. Noisy environments, which manifest themselves with high flux rates, can be mitigated by fast electronics, short sample windows, and thin strip-lines.

Acknowledgments

I would like to thank Henry Frisch for advising the project and providing guidance and encouragement beyond expectation. I would also like to thank Mircea Bogdan, Craig Harabedian, and especially Eric Oberla for their advice and assistance in working with the electronics. I would also like to thank Mary Heintz for keeping the shop running. I acknowledge assistance from Matt Wetstein and Andrey Elagin in data collection and useful conversations. Lastly, I acknowledge assistance and useful conversation from Aaron Meyer, particularly related to the operation of the digital card.

[1] T. Credo, H. Frisch, H. Sanders, and R. Schroll, Picosecond time-of-flight measurement for colliders using Cherenkov light, IEEE Symposium Conference Record Nuclear Science, (2004), http://ieeexplore.ieee.org/lpdocs/epic03/wrapper.htm?arnumber=1462263.

[2] J. Anderson et al., The Development of Large-Area Fast Photo-detectors, (2009), http://hep.uchicago.edu/~frisch/talks/Project_description_nobudgets.pdf.

[3] H. Kim, C.-T. Chen, H. Frisch, F. Tang, C.-M. Kao, An application of micro-channel plate photomultiplier tube to positron emission tomography, (2011), http://psec.uchicago.edu/library/doclib/documents/177/sendit.

[4] H. Frisch, Progress in developing large-area high resolution photo-detectors (LAPPD), (2011), http://hep.

uchicago.edu/~frisch/talks/Ant11_v16.pdf.

[5] H. Kim, C. Kao, H. Frisch, W.W. Moses, W. Choong, J. Genat, F. Tang, and C. Chen, A design of PET detector using microchannel plate PMT with transmission line readout, 2009 IEEE Nuclear Science Symposium Conference Record, (2009), http://ieeexplore.ieee.org/lpdocs/epic03/wrapper.htm?arnumber=5401676.

[6] E. Oberla, Electronics for a Position & Time Sensing Large Area Photo-Detector System (2011), https://indico.fnal.gov/getFile.py/access?contribId=19&sessionId=4&resId=0&materialId=slides&confId=4887.

[7] A. Meyer, Timing analysis on fast pulses in a picosecond resolution photodetector, (2011).

[8] B. Adams, A. Elagin, R. Obaid, E. Oberla, A. Vostrikov, M. Wetstein, 8" MCP timing analysis with PSEC4: data from March 1, 2012, (2012), https://psec.uchicago.edu/blogs/lappd/wp-content/uploads/2012/03/psec4_2012_03_01.pdf